Materials Advances

ROYAL SOCIETY OF CHEMISTRY

PAPER

View Article Online
View Journal | View Issue

Cite this: *Mater. Adv.*, 2024, 5, 1736

Efficient and highly biocompatible 8-arm PEG-Chlorin e6 nanosystems for 2-photon photodynamic therapy of adrenergic disorders†

Natalie S. Potter,[a] Zhen Wang,[b] Evan C. Bornowski,[a] Scott D. Swanson,[c] John P. Wolfe,[a] Alan McLean *[a] and Raoul Kopelman[a]

Received 5th October 2023,
Accepted 5th January 2024

DOI: 10.1039/d3ma00812f

rsc.li/materials-advances

Two highly biocompatible nanosystems have been designed, synthesized, characterized, and demonstrated *in vitro* for enhanced 2-photon photodynamic therapy (2p-PDT) of adrenergic disorders. These systems consist of a compact, star-shaped, 8-arm poly(ethylene glycol) (8-arm PEG) core, to which are attached (1) a natural photosynthetic unit, Chlorin e6 (Ce6), and (2) a choice of two newly synthesized meta-iodobenzylguanidine (MIBG) moieties modified with a 3-mercaptopropionic amide functional linking group "3-MPAM": "MIBG-3-MPAM" or "BG-3-MPAM". A modest self-assembly of these multifunctional nanosystems promotes a 2-photon absorption cross-section (TPACS) enhancement while retaining a high level of reactive oxygen species (ROS) generation. The photodynamic effect of the 8-arm PEG-Ce6-dMIBG nanosystem is shown to be highly effective, while employing harmless, but deep-tissue penetrating, near-infrared (NIR) photons *in vitro* on a neuroblastoma cell line. Thus, this new nanosystem with the dMIBG modification shows high promise towards 2-photon photodynamic therapy of adrenergic diseases, with a wider application on other hard-to-treat diseases.

1 Introduction

There is a growing interest in improving medical outcomes by developing localized phototherapeutics for the treatment of cancer,[1,2] cardiovascular diseases,[3,4] and ocular disorders.[5] Nanoparticle (NP)-assisted delivery is one of the most promising avenues for advances into localized and stimulus-activated therapy.[6–8] NPs are ideal therapeutic agents due to the enhanced permeability and retention (EPR) effect, also known as passive targeting, which accounts for their non-targeted accumulation in diseased regions.[9,10] However, passive targeting alone is usually dependent on the tumor environment and this often limits the NP concentration accumulated at the tumor site, thus resulting in low therapeutic efficacy.[11–13] To improve tumor accumulation and localization surface modifications such as small molecule enhancements has become an attractive avenue.[14,15] Some NPs, such as biocompatible poly(ethylene glycol) (PEG) polymer NPs, are ideal systems for enhanced localization of therapeutics due to their ease of surface conjugation with enhancement moieties, water-solubility, nonspecific biological interactions, and long circulation time.[16–20]

Most notably, many PEG NP systems are known to also have no dark toxicity, *i.e.*, no toxicity in the absence of photons, and are found to have a particular advantage *in vivo* due to their "stealth"-like behavior to bypass molecular recognition by the immune system in biological environments – both highly essential characteristics for biomedical applications.[16,19] There are many other factors to consider when designing PEG NPs as drug delivery or therapeutic systems such as molecular weight (MW), size, shape, surface charge, and stiffness of the delivery platform.[21] Most notably, recent work by Caruso and co-workers investigated the bio-nano interactions of different multi-arm PEG particles and found that the polymer architecture plays an important role in determining whether there are positive or negative interactions with human blood.[19] Another noteworthy property of the multi-arm PEG particle is the wide variety of modifications that can be made to their structure so as to achieve desirable behaviors.[22,23] For instance, Bhatia and coworkers found that utilizing a non-reducible maleimide-linker could lead to a higher delivery efficiency in cultured cells.[24] In our work, the PEG arms were subsequently modified with long non-reducible PEG linkers, so as to not only conjugate the newly synthesized moieties, but also to increase stealth-like behavior and further improve the delivery of the photosensitizer (PS) (Fig. 1).[25]

[a] *Department of Chemistry, University of Michigan, 930 N. University Ave., Ann Arbor, MI 48109, USA. E-mail: ammclean@umich.edu*
[b] *Melville Laboratory for Polymer Synthesis, Yusuf Hamied Department of Chemistry, University of Cambridge, Lensfield Road, Cambridge CB2 1EW, UK*
[c] *Department of Radiology, Michigan Medicine, University of Michigan, 1500 East Medical Center Dr, Ann Arbor, MI 48109, USA*

† Electronic supplementary information (ESI) available. See DOI: https://doi.org/10.1039/d3ma00812f

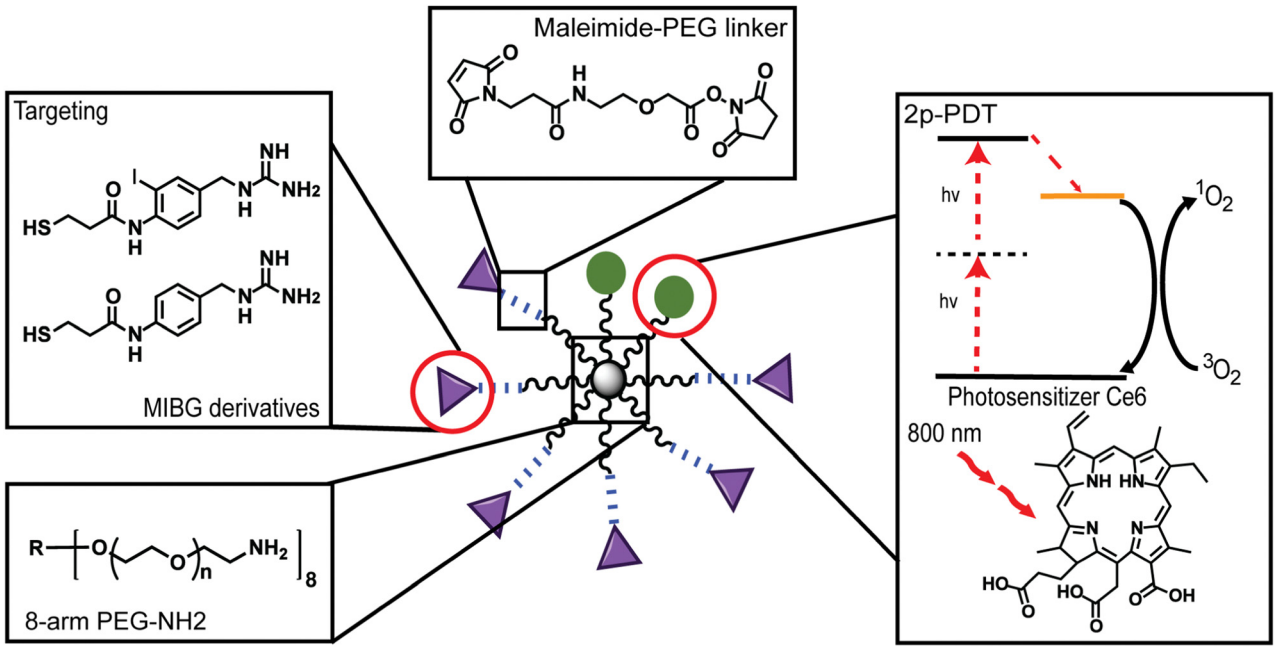

Fig. 1 Fully assembled 8-arm PEG-Ce6-dMIBG/dBG nanosystem depicting the individual components ((left-right clockwise) 8-arm PEG-NH_2; targeting moieties – MIBG-3-MPAM (top) and BG-3-MPAM (bottom); maleimide-PEG linker (MAL-PEG); and 2p-PDT PS – Chlorin e6).

Multi-arm PEG NPs are also highly promising modalities for stimulus-activated therapeutics, such as photodynamic therapy (PDT).[26] Despite the many advantages multi-arm PEG NPs possess there are few studies that report using multi-arm PEG nanoparticles designed for PDT application and of those studies that exist, to our knowledge, only two groups were found to utilize the monomolecular form of 8-arm PEG in the synthesis as the main nanocarrier structure.[3,23,27,28] PDT is a molecular phototherapy in which photons are used to excite a dye molecule, defined as a photosensitizer (PS), which transfers energy from the dyes excited state (ES) to ground-state triplet oxygen molecules (O_2), *i.e.*, "normal" O_2, so as to produce reactive oxygen species (ROS), such as singlet O_2[29] While ROS are naturally produced in the body, an excessive amount is cytotoxic. This cytotoxicity is used by PDT to elicit the death of anomalous, pathology driving cells (*e.g.*, cancer cells) that reside in highly selective targeted tissue regions. Traditional PDT paradigms mostly employ orange-red visible light, with wavelengths of 600–700 nm, because these "redder" photons penetrate deeper into biological tissue.[29,30] However, so as to further improve the photon penetration depth and increase spatial selectivity, 2-photon photodynamic therapy (2p-PDT) has emerged as an exciting methodology.[31] In 2p-PDT, two low-energy near-infrared (NIR) photons, which have minimal tissue scattering and very deep tissue penetration, are used to excite the PS, in a nonlinear optical process, still leading to the production of the ROS.[30,32]

Although 2-photon absorption (TPA) has been used widely in the biomedical field for decades for microscopy, deep-tissue simulation, and localized release of bio-active compounds, few 2-photon PSs have been developed for PDT applications.[31,33–38] For 2p-PDT a sensitizer should have highly efficient NIR excitability (high absorption cross-section). Additionally, an effective PS should have a high ROS quantum yield (also referred to as ROS efficacy) as well as the low dark cytotoxicity, as mentioned previously.[39] The algae photosynthetic unit, Chlorin e6 (Ce6), is an FDA approved (FDA UNII: 5S2CCF3T1Z), second-generation PS and has been reported to be an effective PS not only as a one-photon PDT, but it has also been reported to have strong TPA.[40,41] Thus, this PS has been shown to produce ROS efficiently when excited by either one-photon or 2-photon light.[42] Furthermore, Ce6 can also be readily conjugated to NP surfaces, using a well-known DCC/NHS activation method.[28,43] Due to these advantages, as well as its reported biocompatibility, this natural Ce6 PS seems to be a strong candidate for this 2p-PDT study.

In this work, for enhanced uptake, two *de novo* conjugatable meta-iodobenzylguanidine (MIBG)-derivatives are synthesized. Each of these *de novo* derivatives, as well as the 2-photon active Ce6, are NP-conjugated, for use in enhanced 2p-PDT of adrenergic disorders, *i.e.*, of the sympathetic nervous system. MIBG is a guanethidine analogue modeled on norepinephrine, which is a prominent adrenergic hormone and neurotransmitter recycled by the norepinephrine transporter (NET) within the peripheral nervous system (PNS) and central nervous systems (CNS).[44,45] Due to this, MIBG has historically been used to target NETs for imaging and therapy applications.[46] MIBG molecules traditionally contain a radiolabeled iodine atom and have been previously used for both radio-imaging and radiation treatment of neuroendocrine tumors, such as neuroblastoma and other adrenergic dysfunctions, due to its high molecular affinity for adrenergic-rich tissues[45–47] However, by using the conventional radiolabeled MIBG molecule, its

radioactive iodine atom is undesirable from a health safety perspective. In particular, although controlled clinically, there is still a potential for unforeseen health side effects such as hyperthyroidism, myelosuppression, and bone marrow depression, reportedly associated with the use of ^{123}I/^{131}I-MIBG in clinical trials.[48–50] Thus, in this study, two new MIBG analogues that eliminate the radiolabeled iodine atom and allow for easy conjugation through a thiol linkage were utilized.

Overall, we report the development and application of an 8-arm-PEG NP with both an imaging/photodynamic component using a Ce6 moiety and with an enhancement component using MIBG-derivatives, simultaneously (Fig. 1). The characterization of the nanosystems has been performed through spectroscopy and microscopy methods. Specifically, the loading efficiency of the Ce6 was determined through spectral absorbance, and the conjugation ratios of the MIBG-derivatives were determined through proton diffusion-ordered spectroscopy (^{1}H DOSY). Furthermore, the 2p-PDT potential of the Ce6 moiety was confirmed by calculating the 2-photon absorption cross-section (TPACS) of the free Ce6 and Ce6 attached to the nanosystems as well as through the calculation of the ROS efficacy. Lastly, we demonstrated the 2p-PDT effects of these nanosystems *in vitro*, showing high potential towards *in vivo* deep-tissue photodynamic therapy of adrenergic disorders.

2 Results and discussion

2.1 Synthesis and characterization of 8-arm PEG-Ce6-dMIBG/dBG nanosystems

For the creation of the 8-arm PEG-Ce6 nanosystem, Ce6 conjugation was done through an DCC/NHS activation.[28,51] The exact site of attachment cannot be determined from NMR alone as the overlap of signals prevents the Ce6 carboxyl signals from being deconvoluted. Therefore, the formation of the three possible isomers is presumed moving forward.[52,53] The conjugation of our MIBG derivatives (synthesis found in ESI† Methods and Scheme S1), *N*-(4-(guanidinomethyl)-2-iodophenyl)-3-mercaptopropanamide (MIBG-3-MPAM) and *N*-(4-(guanidinomethyl)phenyl)-3-mercaptopropanamide (BG-3-MPAM), to the 8-arm PEG-Ce6 complex was done through a maleimide-PEG-succinimidyl NHS ester (MAL-PEG-SCM) linker. Through the use of standard peptide protection and deprotection steps and other reaction mechanisms further described in the supporting information, the final molecules were successfully synthesized with stable thioether linkages ("MIBG-3-MPAM" and "BG-3-MPAM" are denoted as "dMIBG" and "dBG" when conjugated to the 8-arm PEG system) (Fig. 2).[54] The structures and purity of the precursors, 8-arm PEG-NH_2 and MAL-PEG-SCM, were verified before synthesis (Fig. S1–S6, ESI†) and final products were verified through nuclear magnetic resonance (NMR) and mass spectrometry methods (MS) (ESI†).

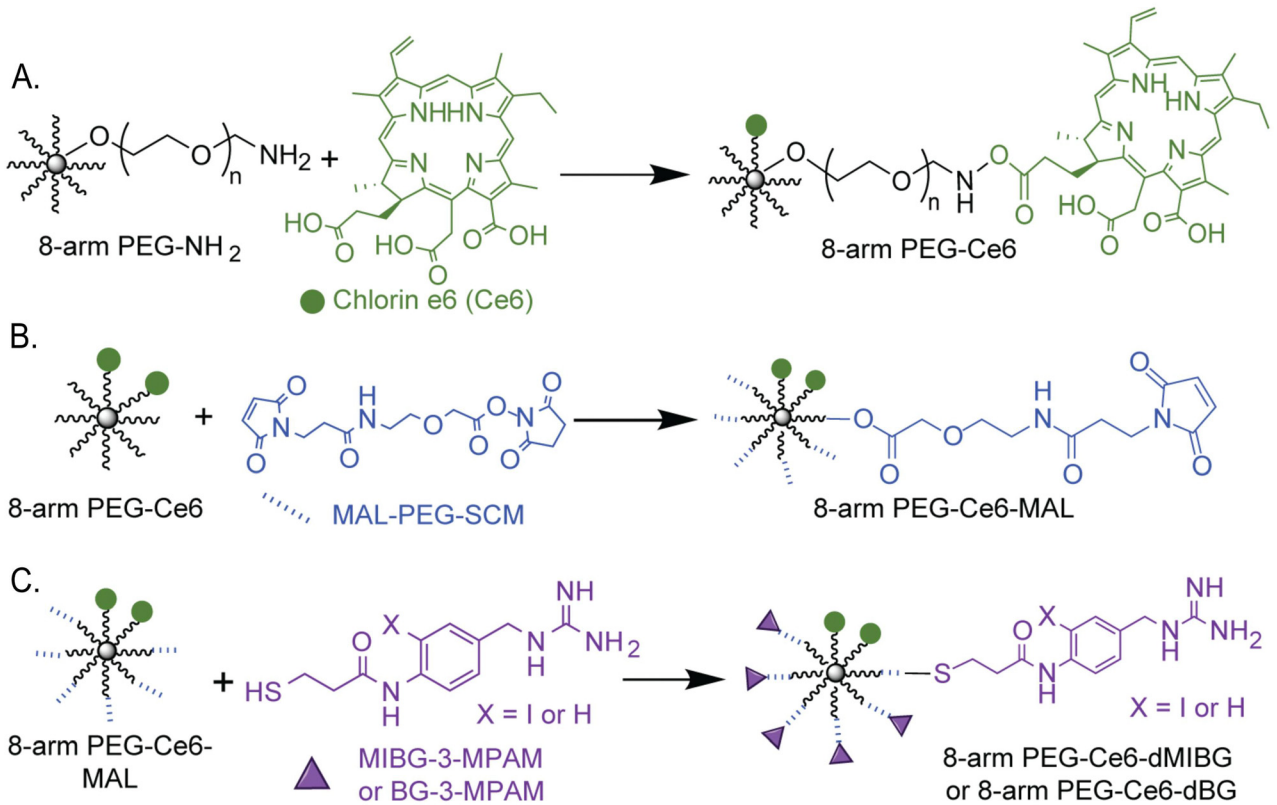

Fig. 2 Chemical synthesis scheme of (A) 8-arm PEG-Ce6 through a DCC/NHS reaction (B) and (C) 8-arm PEG-Ce6-dMIBG/dBG nanosystems with a MAL-PEG-SCM linker to attach the dMIBG/dBG used in this study for 2-photon photodynamic therapy (2p-PDT) applications. Full synthetic details can be found in the ESI† (Section S1 p. 3). We note that the depiction of the Ce6 attached at the middle carboxyl is one of three possible regioisomers that can form.

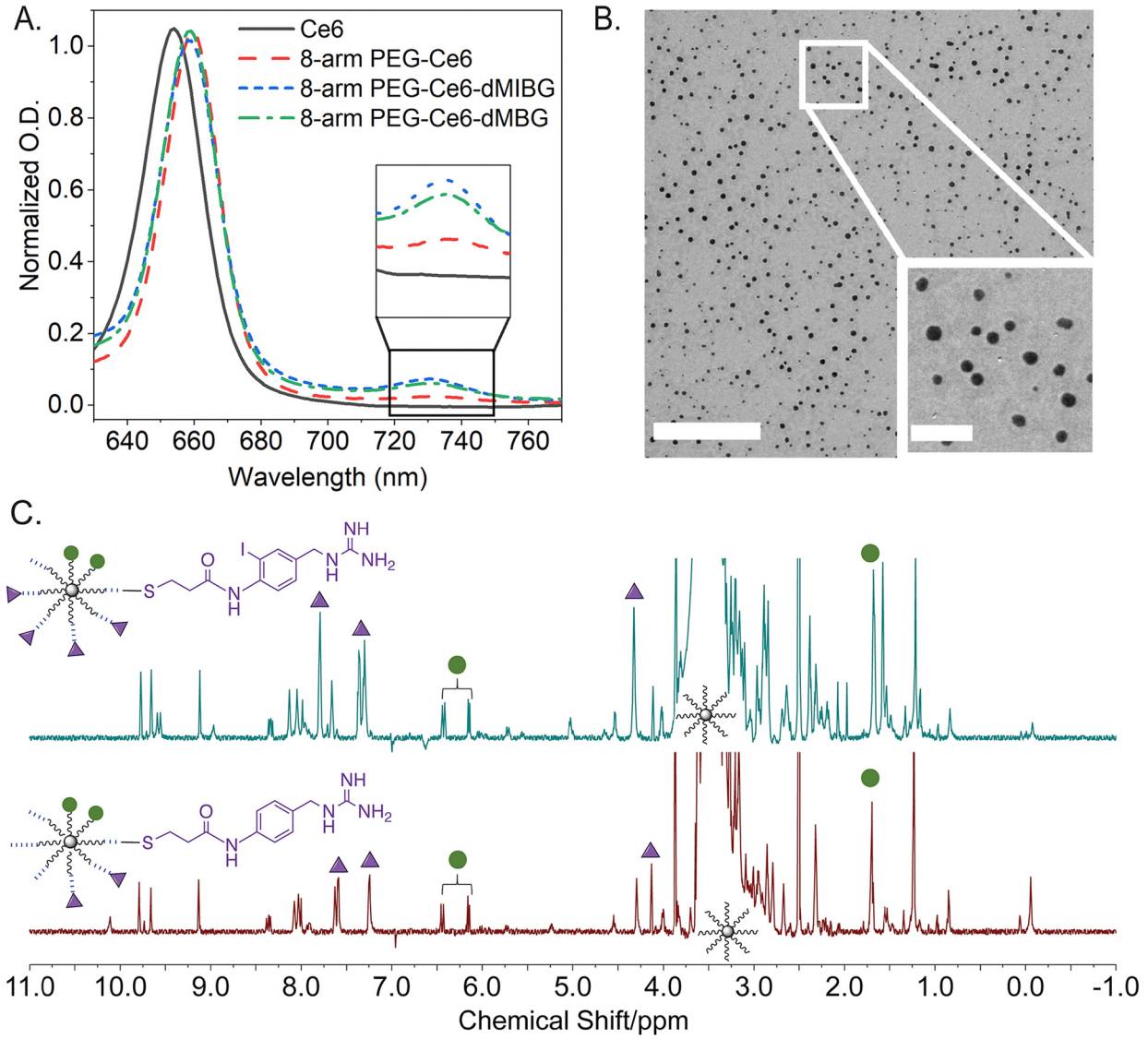

Fig. 3 (A) UV-Vis of free Ce6, 8-arm PEG-Ce6, 8-arm PEG-Ce6-dMIBG, and 8-arm PEG-Ce6-dBG, showing peak shifts around 660 nm and the appearance of some absorbance at 730 nm. (B) TEM of 8-arm PEG-Ce6-dMIBG. Scale bars = 1000 nm and 200 nm (inset). (C) ^{1}H DOSY of assembled nanosystems (8-arm PEG-Ce6-dMIBG, 8-arm PEG-Ce6-dBG) in $DMSO_{d6}$ with Ce6 and dMIBG/dBG characteristic peaks highlighted. Green circle = Ce6 and purple triangle = dMIBG/dBG.

To characterize the nanosystems, UV-Vis spectroscopy (UV-vis), transmission electron microscopy (TEM), proton nuclear magnetic resonance (^{1}H NMR), proton diffusion-ordered spectroscopy (^{1}H DOSY), and gel permeation chromatography (GPC) were employed. UV-Vis and ^{1}H DOSY, paired with a quantitative NMR (qNMR) analysis method, were specifically used to verify the success of the conjugation reactions and quantify the molar conjugation ratios of each molecule. As reported previously by Avula *et al.* through UV-Vis, it was observed that a loaded 8-arm PEG-Ce6 shows shifts of its three absorption maxima when compared to free Ce6 – thereby indicating a successful conjugation of Ce6 to 8-arm PEG (Fig. 3A and Fig. S7, ESI†).[3] While the Soret band around 402 nm shows no significant peak shift, the 504 nm Q-band shows a slight blue-shift towards 501 nm. A Q-band red-shift from 654 nm to 660 nm and the appearance of a 730–735 nm absorbance indicates the successful conjugation of the Ce6. This peak between 730–735 nm then becomes further apparent once the 8-arm PEG-Ce6-dMIBG/dBG complexes are formed.

For the conjugation ratio calculation of the Ce6 to the 8-arm PEG, the lambda max (λ_{max}) from 654 to 660 nm was used (Fig. 3A). Using a calibration curve of Ce6 (in 1× PBS 0.01 M phosphate buffer saline) at 660 nm, it was determined that there are roughly 2.01 ± 0.19 mol of Ce6 per 1 mol of 8-arm PEG (Fig. S8, ESI†). This result is comparable to our previous work, which found the molar ratio to be 1 to 2 molecules of Ce6 per 8-arm PEG.[3] This ratio is assumed to be the same for the 8-arm PEG-Ce6-dMIBG and 8-arm PEG-Ce6-dBG, as the Ce6 conjugation is done through a cross-linking reaction, which is considered to be permanent.[3]

Table 1 Estimated sizes of 8-arm PEG-NH_2, 8-arm PEG-Ce6, 8-arm PEG-Ce6-dMiBG, and 8-arm PEG-Ce6-dBG *via* ^{1}H DOSY (and TEM) at 1 mg mL^{-1}

Compound	Size (nm)
8-arm PEG-NH_2	11.4 ± 1.6 (D_2O)
8-arm PEG-Ce6	19.5 ± 1.7 ($DMSO_{d6}$)
8-arm PEG-Ce6-dBG	18.1 ± 2.5 ($DMSO_{d6}$)
8-arm PEG-Ce6-dMIBG	17.5 ± 1.4 ($DMSO_{d6}$) (16.8 ± 8.1(TEM))

While the ratio of the Ce6 to 8-arm PEG was determined through optical absorbance, it was necessary to use ^{1}H DOSY to first calculate the average molar ratios of dMIBG or dBG to Ce6 in order to determine the conjugation ratios of dMIBG/dBG to 8-arm PEG. This was possible through the identification and integration of characteristic peaks for Ce6 and dMIBG/dBG (Fig. 3C and Fig. S9, S10, Tables S1a–S2b, ESI†). Thus, through this method, the average molar ratios of dMIBG or dBG to 8-arm PEG were determined to be 5.50 ± 0.90 mol and 3.26 ± 0.45 mol per 1 mol of 8-arm PEG, respectively.

For the size analysis, the TEM measurements for this 8-arm PEG-Ce6-dMIBG sample show an average diameter size of 16.8 nm. This result is larger than previous measurements of the 8-arm PEG-NH_2 (the skeletal multi-arm PEG structure), which was found to be between 10–12 nm measured *via* TEM.[28] This increase can largely be attributed to the addition of 6 MAL-PEG chains to the 8-arm PEG backbone structure and to the small molecules. Through this method, only the 8-arm PEG-Ce6-dMIBG samples were able to be successfully analyzed, due to the presence on the complex of the iodine atom, which enhanced the NP contrast over the background (Fig. 3B). The samples of 8-arm PEG-Ce6 and 8-arm PEG-Ce6-dBG could not be easily distinguished from their background (Fig. S11, ESI†). Therefore, ^{1}H DOSY was additionally used to calculate the sizes of the 8-arm PEG-Ce6, 8-arm PEG-Ce6-dBG, and 8-arm PEG-Ce6-dMIBG and to further verify the formation of the final nanosystems.

Through ^{1}H DOSY measurements we were also able to show an increase in size once the 8-arm PEG-NH_2 was modified with Ce6 (Table 1), but a decrease in size once the PEG linker and the small molecules (MAL-PEG-SCM and dMIBG/dBG) were conjugated to the 8-arm-PEG-Ce6 structure (Fig. S2, ESI†). The observed variation in particle sizes of the 8-arm PEG-Ce6-dMIBG in the TEM image further suggests that in the final NP formation, there is some assembly-like behavior occurring (ESI† Section S2). It is crucial to note that even for the largest assemblies, the average diameter of the particles remains under 100 nm. Therefore, while we further investigated the size properties of the PEG nanosystems through GPC (Fig. S12, ESI†), the <100 nm size of all the NPs variants indicates a desirable range for *in vivo* applications.[22,25]

2.2 2p cross-section and reactive oxygen species efficacy

A large TPACS and high ROS efficacy are ideal characteristics for a PS or stimulus-activated nanosystem.[55] The 2-photon excited fluorescence (TPEF) method, which is based on power dependent fluorescence emission collection, is considered to be the most reliable method, compared to the Z-scan method.[56,57] This is due to its high fluorescence emission collection, high accuracy (lower likelihood of an overestimation), and ability to deconvolute the 1-photon from the combined 2-photon + 1-photon effects when a non-pulsed laser is used to excite the samples (Fig. 4A and Fig. S13, ESI†).[58] Utilizing the TPEF method, the 2-photon power dependent fluorescence emission in the range of 650–690 nm was thus collected. After isolating the 2-photon effects, the log–log power dependence of all the Ce6 variants was found to have slopes of 2 (two), within error (Fig. S14, ESI†). This indicates that the fluorescence originates from pure TPA.[57] All these trials concerning the power dependent TPA fluorescence are provided, for all the Ce6 NP complexes, in the ESI† (Fig. S15).

The moderate TPACS *y*-intercepts, across all samples (Fig. S14, ESI†), ranging from 4.4 to 4.6, indicate reasonably sized TPACS for all the Ce6-NP complexes. The resulting cross-section (''action cross-section''), when using the TPEF method, is the product of the fluorescence quantum yield and the TPACS. Due to our previous suggesting that some assembly is occurring due to π-stacking of the Ce6 molecules, the fluorescent quantum yields cannot be assumed to be consistent between samples.[59–61] With the quantum yields calculated, we determined the TPACS of free Ce6, 8-arm PEG-Ce6, and 8-arm PEG-Ce6-dMIBG/dBG (Fig. 4B, Fig. S16 and Table 2, ESI†). With an experimental cross-section of 24 ± 8 GM the free Ce6 was found to have the smallest cross-section, which was further found comparable to a previously reported value of 33.6 GM by the application of the Z-scan method, which can result in an overestimation of the cross-section.[42,62] It was observed that while there was an increase in the TPACS to 56 ± 2 GM, when the Ce6 molecules were conjugated to the 8-arm PEG and there was an increase once the small molecules were conjugated, there was no significant difference in the cross-section values between the 8-arm PEG-Ce6-dBG and the 8-arm PEG-Ce6-dMIBG nanosystems themselves (72 ± 23 GM and 78 ± 25 GM, respectively). An enhancement of the TPACS may be due to the emergence of a peak at approximately 730–735 nm appearing near the 2-photon virtual-state transition at 800 nm when Ce6 is conjugated to PEG, the peak becoming further enhanced upon the MAL-PEG-dMIBG/dBG conjugation (Fig. S7, ESI†). States near-resonance to virtual state transitions are known to strongly enhance the rate of TPA.[63,64]

To determine the ROS production of the 8-arm PEG-Ce6-dMIBG/dBG nanosystems and of the free Ce6 the reactive oxygen sensing probe singlet oxygen sensor green (SOSG), was used to indirectly measure the ROS production because of its ability to react with singlet oxygen ($^1O_2$).[65,66] SOSG has been previously employed to detect $^1O_2$ production of Ce6 using a 660 nm excitation, but to our knowledge a 400 nm excitation, in particular, has yet to be used to evaluate the ROS production of Ce6.[67,68] An increasing fluorescence intensity was observed as the total irradiation time increased, indicating the successful production of $^1O_2$ (Fig. 4C, D and Fig. S15, ESI†).

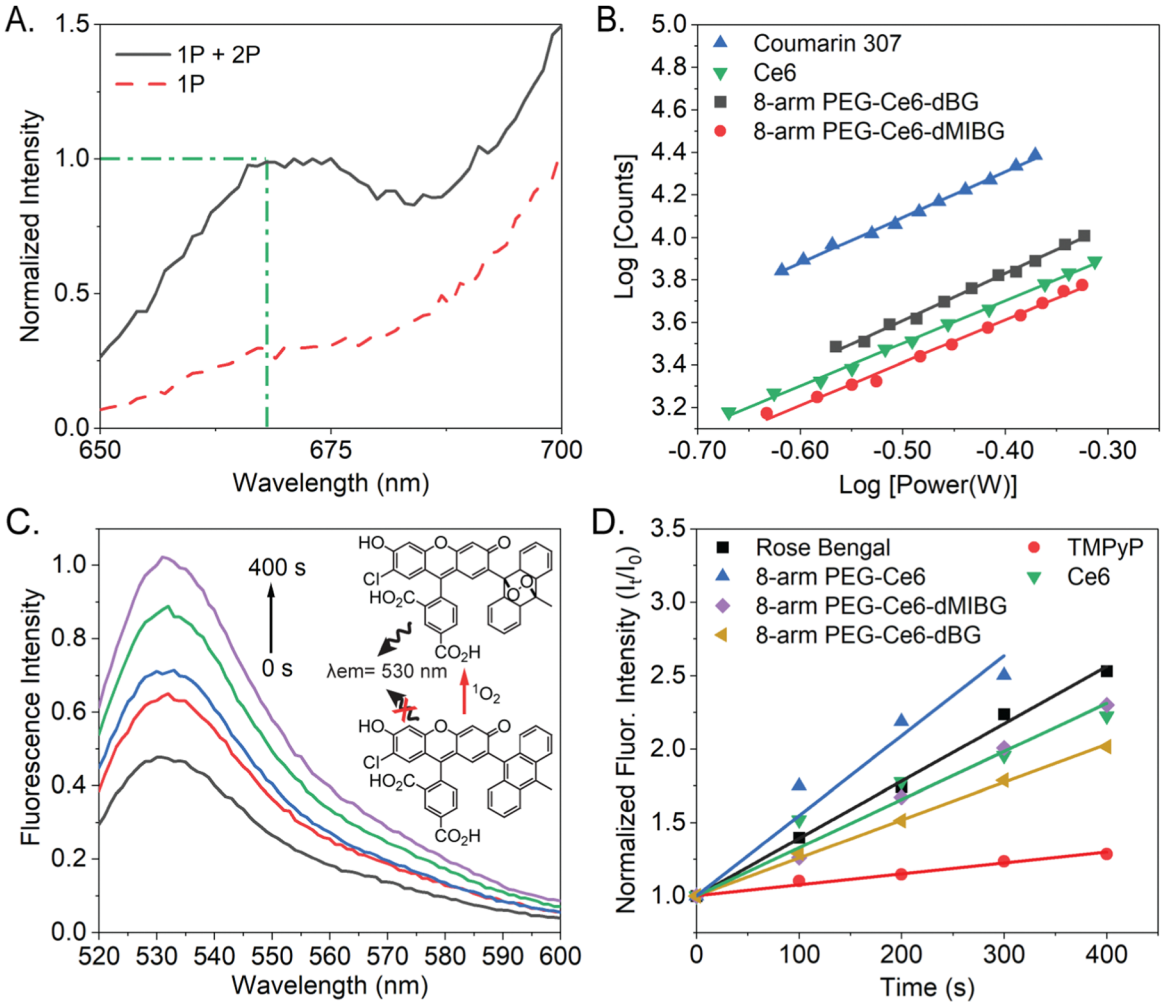

Fig. 4 (A) Showing the combined 2-photon + 1-photon stimulated fluorescence from Ce6 in contrast to the 1-photon fluorescence at 668 nm (indicated by green dotted line) from a 800 nm laser set to 0.383 W. (B) 2-photon log[Counts] *vs.* log[Power (W)] graph of Coumarin 307 at 506 nm, 8-arm PEG-Ce6-dMIBG, and 8-arm PEG-Ce6-dBG at 668 nm to calculate the 2-photon cross section. (C) Emission spectra of 8-arm PEG-Ce6-dMIBG + SOSG after excitation at 400 nm showing the increase in SOSG-EP fluorescence. (D) Normalized fluorescent intensity of SOSG-EP at 530 nm after continuous illumination of 0–400 s at 549 nm (Rose Bengal – RB) and at 400 nm (Ce6, 8-arm PEG-Ce6, 8-arm PEG-Ce6-dMIBG, and 8-arm PEG-Ce6-dBG), used to calculate the ROS efficacies.

Table 2 TPACS and ROS efficacy values for free Ce6, 8-arm PEG-Ce6 and 8-arm PEG-Ce6-dBG/dMIBG

Compound	TPACS (GM)	ROS efficacy[a] (%)
Ce6	24 ± 8	63 ± 8
8-arm PEG-Ce6	56 ± 2	94 ± 16
8-arm PEG-Ce6-dBG	72 ± 23	49 ± 16
8-arm PEG-Ce6-dMIBG	78 ± 25[b]	63 ± 4

[a] All experiments were done in triplicate (n = 3). [b] All TPACS experiments were repeated n = 3 except for the 8-arm PEG-Ce6-Dmibg (n = 4).

We conducted detailed studies to quantify the ROS efficacy (Table 2) and saw an increasing fluoresence intensity as the total irradiation time increased, indicating the successful production of $^1O_2$ (Fig. 4C, D and Fig. S15, ESI†). The ROS of all variants is high (>50%), indicating that the PEG platforms are well-suited for photodynamic therapy applications. There is modest variation in ROS efficacy between samples, attributed to effects of the small molecule moiety and heavy atom effect (ESI† Section S2).[69–73] These findings illustrate a fascinating realtionship between the different nanosystem design and their resulting 2-photon cross section (up to 3× enhancement) and ROS efficacy.

2.3 *In vitro* cytotoxicity of 8-arm PEG nanosystems

Good biocompatibility without illumination, *i.e.*, the absence of "dark toxicity," should be required when choosing a therapeutic agent for PDT applications. The biocompatibility of Ce6 has been widely reported, but with varying results.[74–79] Therefore, to further investigate the biocompatibility of the free Ce6 and the other Ce6-NP complexes, a colorimetric assay was conducted using 3-(4,5-dimethylthiazol-2-yl)-2,5-diphenyltetrazolium bromide (MTT) (Fig. 5).[80] We saw a significant decrease in viability as the concentration of free Ce6 increases when cells were incubated with only the free Ce6 and the 8-arm PEG Ce6, even at the low concentration of 2 μM. All cell viability was

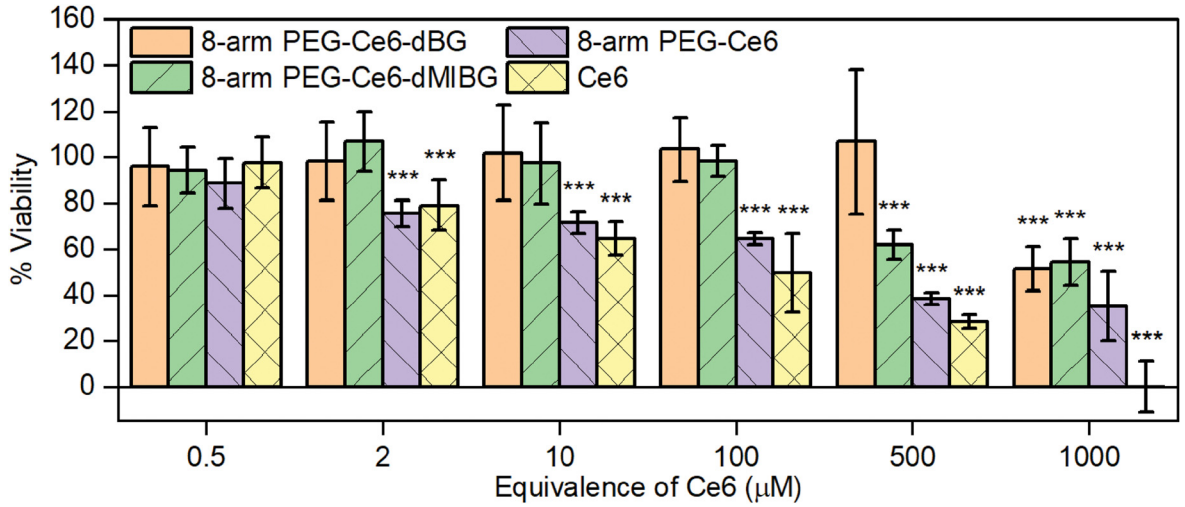

Fig. 5 (A) Cell viability of SK-N-BE(2)C neuroblastoma cells with Ce6, 8-arm PEG-Ce6, 8-arm PEG-Ce6-dMIBG, and 8-arm PEG-Ce6-dBG at varying concentrations (2, 10, 100 μM equiv. of Ce6). Data is presented as mean ± SD (n = 5). Significance was calculated *via* student-t test ***$P < 0.001$ compared to control samples with 100% viability.

eliminated at a free Ce6 concentration of 1000 μM, and when exposed to 8-arm PEG-Ce6 the viability was decreased to about 35% at the same concentration. Conversely, once the Ce6 is conjugated to the 8-arm PEG, the decrease in average viability was only to around 50%, at the highest Ce6 concentration. However, once the small molecules (dBG and dMIBG) are conjugated to the system, the viability remains at 97% or above up to 100 μM. Once a 500 μM equivalence of Ce6 was reached the 8-arm PEG-Ce6-dMIBG started to show significant toxicity, reducing the cell viability to 60%. Notably, the 8-arm PEG-Ce6-dBG showed little cytotoxicity at all concentrations except for the highest, 1000 μM equivalent Ce6, concentration. These significant results show that the Ce6 cytotoxicity is significantly reduced once conjugated to the 8-arm PEG, thus becoming more biocompatible, over a wider range of concentrations, and even more so once the PEG-small molecule linkages are attached. Additionally, even though both 8-arm PEG-Ce6-dMIBG and -dBG nanosystems remain biocompatible, even at higher concentrations, the iodine attached to the molecule appears to have only a minor impact on the biocompatibility of the entire nanosystem. This low cytotoxicity is indicative of a highly desirable therapeutic, and thus is a very significant result of this investigation.

2.4 *In vitro* 2p-PDT

To assess the application potential of the 8-arm PEG-Ce6-dMIBG nanosystem, which showed the most promising results from the previous section *in vitro* 2p-PDT tests were performed on the SK-N-BE(2)C neuroblastoma cell line, which was chosen due to its specific uptake of norepinephrine and its high endogenous expression of NETs.[81] Previous studies showed even when attached to nanoparticles, MIBG derivatives target the same uptake-1 mechanism through the NETs.[82,83] This can be presumed to apply to our system as well. The only exception that we have reported is in the instance of excess MIBG, which triggers a nonspecific enhanced uptake.[84] Note that this is not the case for this nanosystem. NPs with a 1 μM equivalence of Ce6 were used for the *in vitro* 2p-PDT experiment, because of their higher dark cell viability over 24 h (Fig. 5). Samples were illuminated with an 800 nm pulsed laser at 2.4 mW for 10 scans (400 Hz speed, 1.2 μm pixel dwell-time) within a 250 μm × 250 μm box (40× objective). These parameters were chosen based on previous *in vitro* 2p-PDT literature.[85–87] However, the protocol was modified to ensure the natural cell death cycle did not skew any results within a 12-h incubation time (full details in Section S1, ESI†). Calcein AM, a fluorescent dye, was used to mark cell viability as it is often employed to study 2p-PDT.[31] A co-stain method with propidium iodide (PI) was also utilized to verify the cell death. The observation of significant decreased Calcein AM fluorescence (a result of cell membrane disruption) combined with the cells' nuclei being positively stained with PI confirms cell death by necrosis (Fig. 6B).[31]

As expected, the control sample incubated with no NPs showed that the NIR radiation did not by itself cause a significant cell kill effect, as there was no PI staining (Fig. 6B). Interestingly, although the 8-arm PEG-Ce6 showed the highest ROS efficacy (Fig. 3D and Table 2), the 8-arm PEG-Ce6 samples showed a minimal amount of disruption to the cell membranes through the presence of PI. Through image analysis the amount of cell death caused by 8-arm PEG-Ce6 was not deemed statistically significant (Section S1 and Tables S3, S4, ESI†). In contrast, statistically significant cell death was observed when the 8-arm PEG Ce6-dMIBG NPs were incubated with the cells and irradiated. This is indicated by the increase in PI staining (Fig. 6B), demonstrating a higher cell kill efficiency due to the stronger photodynamic effects when using the 8-arm PEG-Ce6-dMIBG NPs (Table S3, ESI†). The larger increase for the 8-arm PEG-Ce6-dMIBG nanosystem reveals an advantage of having a strong TPACS and uptake enhancement due to the dMIBG moieties.

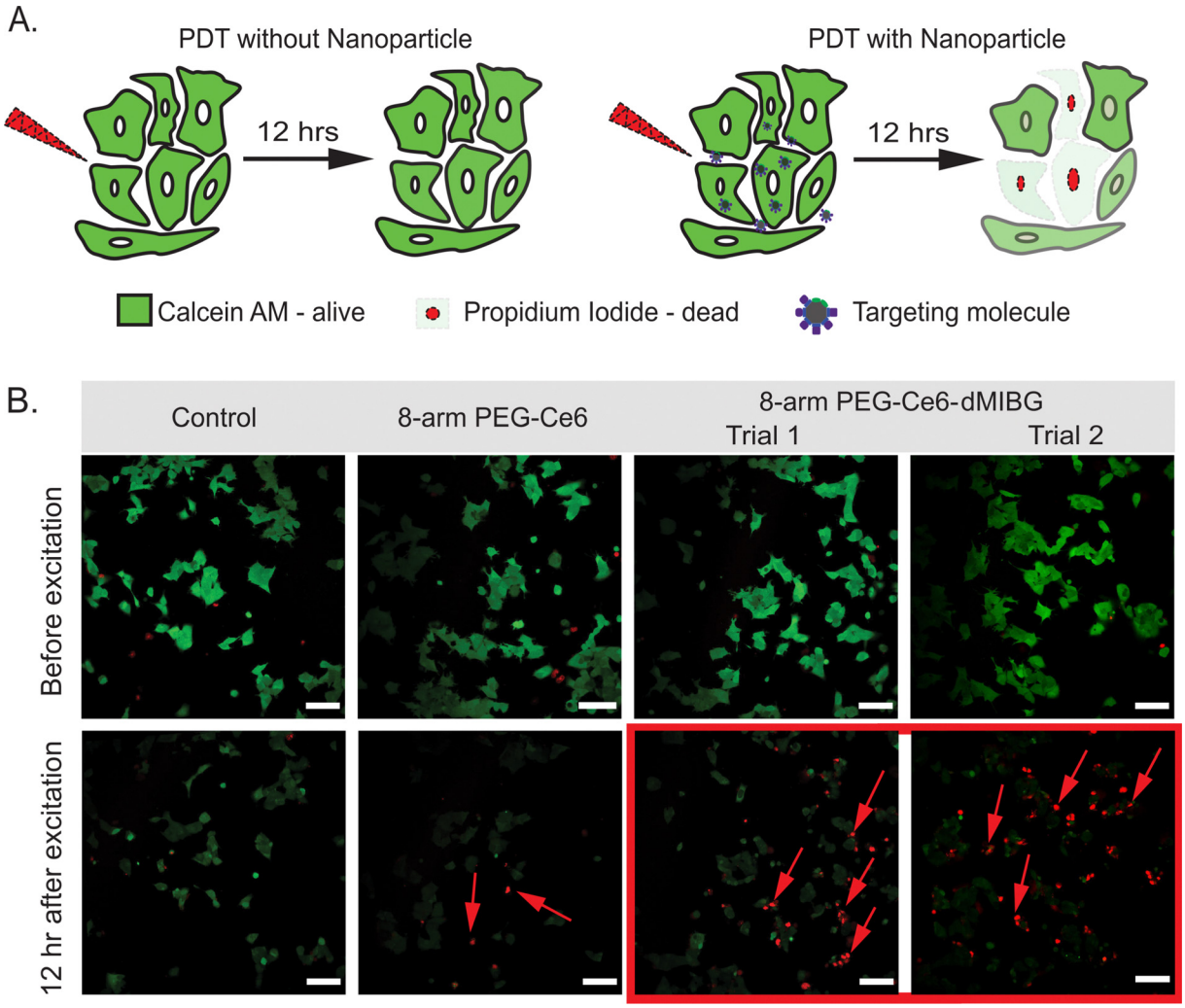

Fig. 6 (A) Illustration showing the 2p-PDT effects without any PS/nanosystem (top) *versus* with the nanosystem (bottom) using Calcein AM and propidium iodide (PI) as co-stains representing cell viability and cell death, respectively. (B) 2p-PDT images of SK-N-BE(2)C cells with control (no NP) as well as 1 μM Ce6 equivalence of 8-arm-PEG-Ce6, and 8-arm-PEG-Ce6-dMIBG (Trials 1 and 2) under 800 nm 2-photon illumination. Samples were co-stained with Calcein AM and PI to indicate cell viability and cell death, respectively. Scale bar is 100 μm. Additional images of control and 8-arm PEG-Ce6 (Trial 2) can be found in Fig. S17 and S18 (ESI†).

3 Conclusions

In this study, we prepared the 2-photon photosensitizer Ce6 and two novel non-radioactive MIBG molecules conjugated to an ultracompact 8-arm PEG NP so as to create highly effective nanosystems for 2p-PDT of adrenergic disorders. To quantify 2p-PDT potential, we measured the TPACS and ROS quantum yield of the nanosystems. We found that not only were the photosensitization properties of the Ce6 maintained across all PEG platforms – TPACS and ROS efficacy were enhanced when Ce6 was attached to 8-arm PEG due to Ce6 π-stacking and modest NP assembly. Additionally, when conjugating the MIBG derivatives to the 8-arm PEG platform, TPA showed further enhancement. Having demonstrated a high biocompatibility across all samples, we lastly showed that incorporating both Ce6 and the dMIBG onto 8-arm PEG produced the greatest *in vitro* 2p-PDT efficiency far exceeding 8-arm PEG-Ce6 used in isolation. Overall, the multifunctional 8-arm PEG NPs with Ce6 and derivatives of MIBG show great promise towards deep-tissue photodynamic therapy of adrenergic disorders without the use of a conventional radiolabel. Our study also provides an important framework for improving photodynamic therapy efficacy with a 2p-PS tuneability for functional nanoparticles across disease models.

Author contributions

Conceptualization: N. S. P., A. M., and R. K.; methodology: N. S. P., Z. W., E. C. B., S. D. S., and A. M.; formal analysis: N. S. P., S. D. S., and A. M.; investigation: N. S. P., Z. W., and A. M.; visualization: N. S. P.; resources: J. P. W. and R. K.; writing – original draft: N. S. P. and A. M., writing – review and editing: N. S. P., Z. W., A. M., and R. K.; supervision: E. C. B., J. P. W., A. M., and R. K.; project administration: A. M. and R. K.

Conflicts of interest

There are no conflicts to declare.

Acknowledgements

This manuscript is dedicated to Dr Raoul Kopelman (October 21, 1933–July 20, 2023). RK acknowledges the National Cancer Institute for funding support (R01CA186769, R01CA250499). The authors thank the BRCF Microscopy Core at The University of Michigan for providing the equipment and guidance for both the 2p-PDT and TEM work. The authors also would like to thank Prof. Oren A. Scherman, Prof. Silvia Vignolini, and Dr Jade A. McCune at the University of Cambridge for providing the equipment and guidance necessary to run the aqueous gel permeation chromatography (GPC) found in the ESI† of this text.

References

1 J. Shi, P. W. Kantoff, R. Wooster and O. C. Farokhzad, *Nat. Rev. Ccancer*, 2017, **17**, 20–37.
2 K. A. Simmer, H. J. Hah, Y.-E. K. Lee, O. Sagher, D. Orringer, M. Philbert and R. Kopelman, *Int. J. Nanomed. Nanosurg.*, 2015, **1**, 1–13.
3 U. M. R. Avula, H. K. Yoon, C. H. Lee, K. Kaur, R. J. Ramirex, Y. Takemoto, S. R. Ennis, F. Morady, T. Herron, O. Berenfeld, R. Kopleman and J. Kalifa, *Sci. Trans. Med.*, 2015, **7**, 172.
4 R. Pala, V. T. Anju, M. Dyavaiah, S. Busi and S. M. Nauli, *Int. J. Nanomed.*, 2020, **15**, 3741–3769.
5 Y. Weng, J. Liu, S. Jin, W. Guo, Z. Liang and Z. Hu, *Acta Pharm. Sin. B*, 2016, **7**, 281–291.
6 J. D. Byrne, T. Betancourt and L. Brannon-Peppas, *Adv. Drug Delivery Rev.*, 2008, **60**, 1615–1626.
7 Y.-E. L. Koo, G. R. Reddy, M. Bhojani, R. Schneider, M. A. Philbert, A. Rehemtulla, B. D. Ross and R. Kopelman, *Adv. Drug Delivery Rev.*, 2006, **58**, 1556–1577.
8 R. Bazak, M. Houri, S. E. Achy, S. Kamel and T. Refaat, *J. Cancer Res. Clinc. Oncol.*, 2014, **141**, 769–784.
9 S. K. Nune, P. Gunda, P. K. Thallapally, Y.-Y. Lin, M. L. Forrest and C. J. Berkland, *Exp. Opin. Drug Delivery*, 2009, **6**, 1175–1194.
10 H. Kang, S. Rho, W. R. Stiles, S. Hu, Y. Baek, D. W. Hwang, S. Kashiwagi, M. S. Kim and H. S. Choi, *Adv. Healthcare Mater.*, 2019, **9**, 1901223.
11 F. Z. Gu, R. Karnik, A. Z. Wang, F. Alexis, E. Levy-Nissenbaum, S. Hong, R. S. Lager and O. C. Farokhzad, *Nano Today*, 2007, **2**, 14–21.
12 Y. Shi, R. van der Meel, X. Chen and T. Lammers, *Teranostics*, 2020, **10**, 7921–7924.
13 S. D. Steichen, M. Caldorera-Moore and N. A. Peppas, *Eur. J. Pharm. Sci.*, 2013, **48**, 416–427.
14 M. Overchuk, K. M. Harmatys, S. Sindhwani, M. A. Rajora, A. Koebel, D. M. Charron, A. M. Syeda, J. Chen, M. G. Pomper, B. C. Wilson, W. C. W. Chan and G. Zheng, *Nano Lett.*, 2021, **21**, 344–352.
15 A. D. Friedman, S. E. Claypool and R. Liu, *Curr. Pharm. Des.*, 2013, **19**, 6315–6329.
16 J. V. Jokerst, T. Lobovkina, R. N. Zare and S. S. Gambhir, *Nanomedicine*, 2011, **6**, 715–728.
17 W. Qian, T. Curry, Y. Che and R. Kopelman, Proc. SPIE 8595, Collodial Nanocrystals for Biomedical Applications VIII, 2013, vol. 85951D, pp. 715–728.
18 F. Chen, E. B. Ehlerding and W. Cai, *J. Nucl. Med.*, 2014, **55**, 1919–1922.
19 J. Song, Y. Ju, T. H. Amarasena, Z. Lin, S. Mettu, J. Zhou, M. A. Rahim, C.-S. Ang, C. Cortez-Jugo, S. J. Kent and F. Caruso, *ACS Nano*, 2021, **15**, 10025–10038.
20 L. Hao, N. Rohani, R. T. Zhao, E. M. Pulver, H. Mak, O. J. Kelada, H. Ko, H. E. Fleming, F. B. Gertler and S. N. Bhatia, *Nat. Mater.*, 2021, **20**, 1440–1448.
21 W. Poon, B. R. Kingston, B. Ouyang, W. Ngo and W. C. W. Chan, *Nat. Nanotechnol.*, 2020, **15**, 819–829.
22 L. Dai, X. Cao, K.-F. Liu, C.-X. Li, G.-F. Zhang, L.-H. Deng, C.-L. Si, J. He and J.-D. Lei, *J. Mater. Chem. B*, 2015, **3**, 3754–3766.
23 Y. Zhao, F. Li, C. Mao and X. Ming, *Mol. Pharm.*, 2018, **15**, 2559–2569.
24 E. J. Kwon, H. Ko and S. N. Bhatia, *Mol. Pharm.*, 2020, **17**, 3633–3642.
25 K. Liu, L. Dai, C. Li, J. Liu, L. Wang and J. Lei, *Sci. Rep.*, 2016, **6**, 29461.
26 X. Li, J. F. Lovell, J. Yoon and X. Chen, *Nat. Rev. Clin. Oncol.*, 2020, **17**, 657–674.
27 U. Avula, H. Yoon, G. Kim, R. Kopelman and J. Kalifa, *Heart Rhythm*, 2013, **10**, 1747.
28 T. Hopkins, S. D. Swanson, J. D. Hoff, N. Potter, R. Ukani and R. Kopelman, *ACS Appl. Bio. Mater.*, 2018, **1**, 1094–1101.
29 T. J. Dougherty, C. J. Gomer, B. W. Henderson, G. Jori, D. Kessel, M. Korbelik, J. Moan and Q. Peng, *J. Natl. Cancer Inst.*, 1998, **90**, 889–905.
30 T. D. Horvath, G. Kim, R. Kopelman and S. Ashkenazi, *Analyst*, 2008, **133**, 747–749.
31 D. Gao, R. R. Agayan, H. Xu, M. A. Philbert and R. Kopelman, *Nano Lett.*, 2006, **6**, 2383–2386.
32 Z. Zhou, J. Song, L. Nie and X. Chen, *Chem. Soc. Rev.*, 2016, **45**, 6597–6626.
33 M. Pawlicki, H. A. Collins, R. G. Denning and H. L. Anderson, *Angew. Chem., Int. Ed.*, 2009, **48**, 3244–3266.
34 A. McLean, R. Wang, Y. Huo, A. Cooke, T. Hopkins, N. Potter, Q. Li, J. Isaac, J. Haidar, R. Jin and R. Kopelman, *ACS Appl. Nano Mater.*, 2020, **3**, 1420–1430.
35 Y. Li, R. Tang, X. Liu, J. Gong, Z. Zhao, Z. Sheng, J. Zhang, X. Li, G. Niu, R. T. K. Kwok, W. Zheng, X. Jiang and B. Z. Tang, *ACS Nano*, 2020, **14**, 16840–16853.
36 Y. Shen, A. J. Shuhendler, D. Ye, J.-J. Xu and H.-Y. Chen, *Chem. Soc. Rev.*, 2016, **45**, 6725–6741.
37 W.-P. Li, C.-J. Yen, B.-S. Wu and T.-W. Wong, *Biomedicines*, 2021, **9**, 69–90.
38 P. T. C. So, H. Kim and I. E. Kochevar, *Opt. Express*, 1998, **3**, 339–350.
39 A. Gong, F. Meng, J. R. Starkey, B. L. Moss, A. Rebane, M. Drobizhev and C. W. Spangler, *Novel Two-Photon*

Activated Photodynamic Therapy Agents: Design, Synthesis, and Preclinical Studies on Subcutaneous Cancerous Tumors, American Chemical Society, Washington, DC, USA, 1st edn, 2008.
40 M. G. Adimoolam, V. A. M. R. Nalam and M. V. Sunkara, *J. Mater. Chem.*, 2017, **5**, 9189–9196.
41 S. Nasr, M. Rady, A. Sebak, I. Gomaa, W. Fayad, M. E. Gaafary, M. Abdel-Kader, T. Syrovets and T. Simmet, *Pharmaceutics*, 2020, **12**, 494–509.
42 H. Gattuso, A. Monari and M. Marazzi, *RSC Adv.*, 2017, **7**, 10992–10999.
43 H. Abrahamse and M. R. Hamblin, *Biochem. J.*, 2016, **473**, 347–364.
44 N. Pandit-Taskar and S. Modak, *J. Nucl. Med.*, 2017, **58**, 39S–53S.
45 M. Nakajo, K. Shimabukuro, N. Miyaji, J. Shimada, K. Shirono, H. Sakata, H. Yoshimura, R. Yonekura and S. Shinohara, *J. Nucl. Med.*, 1985, **26**, 357–365.
46 S. E. Sharp, A. T. Trout, B. D. Weiss and M. J. Gelfand, *Radiographics*, 2016, **36**, 258–278.
47 S. G. DuBois and K. K. Matthay, *Nucl. Med. Biol.*, 2008, **35**, S35–S48.
48 F. Grünwald and S. Ezziddin, *Semin. Nucl. Med.*, 2010, **40**, 153–163.
49 D. A. Pryma, B. B. Chin, R. B. Noto, J. S. Dillon, S. Perkins, L. Solnes, L. Kostakoglu, A. N. Serafini, M. H. Pampaloni, J. Jensen, T. Armor, T. Lin, T. White, N. Stambler, S. Apfel, V. A. DiPippo, S. Mahmood, V. Wong and C. Jimenez, *J. Nucl. Med.*, 2019, **60**, 623–630.
50 A. Quach, L. Ji, V. Mishra, A. Sznewajs, J. Veatch, J. Huberty, B. Franc, R. Sposto, S. Groshen, D. Wei, P. Fitzgerald, J. M. Maris, G. Yanik, R. A. Hawkins, J. G. Villablanca and K. K. Matthay, *Pediatr. Blood Cancer*, 2011, **56**, 191–201.
51 X. Fu, H. Sun, G. Zhang, K. Zhao, Y. Tian, Z. Gao, J. Cui and Q. Yu, *Colloids Surf.*, 2020, **606**, 125394.
52 H. Chen, R. G. W. Jinadasa, L. Jiao, F. R. Fronczek, A. L. Nguyen and K. M. Smith, *Eur. J. Org. Chem.*, 2015, 3661–3665.
53 M. Vicente and K. Smith, *Molecules*, 2023, **8**, 3479–3491.
54 J. Wang, S. Yang and K. Zhang, *J. Pharm. Biomed. Anal.*, 2018, **164**, 452–459.
55 S. Wang, W. Wu, P. Manghnani, S. Xu, Y. Wang, C. C. Goh, L. G. Ng and B. Liu, *ACS Nano*, 2019, **13**, 3095–3105.
56 Q. Zhang, X. Tian, H. Zhou, J. Wu and Y. Tian, *Materials*, 2017, **10**, 223–260.
57 C. Xu and W. W. Webb, *J. Opt. Soc. Am. B*, 1996, **13**, 481–491.
58 J. Olesiak-banska, M. Waszkielewicz, K. Matczyszyn and M. A. Samoc, *RSC Adv.*, 2016, **6**, 98748–98752.
59 K. Rurack and M. Spieles, *Anal. Chem.*, 2011, **83**, 1232–1242.
60 A. Bouwer, *Pure Appl. Chem.*, 2011, **83**, 2213–2228.
61 C. Wurth, D. Geibler, T. Behnke, M. Kaiser and U. Resch-Genger, *Anal. Bioanal. Chem.*, 2015, **407**, 59–78.
62 P. D. Zhao, P. Chen, G. Q. Tang, G. L. Zhang and W. J. Chen, *Chem. Phys. Lett.*, 2004, **390**, 41–44.
63 L. T. Bergendahl and M. J. Paterson, *Chem. Commun.*, 2011, **48**, 1544–1546.
64 J. Arnbjerg, A. Jiménez-Banzo, M. J. Paterson, S. Nonell, J. I. Borrell, O. Christiansen and P. R. Ogilby, *J. Am. Chem. Soc.*, 2007, **129**, 5188–5199.
65 H. Lin, Y. Shen, D. Chen, L. Lin, B. C. Wilson, B. Li and S. Xie, *J. Fluoresc.*, 2013, **23**, 41–47.
66 S. Kim, M. Fujitsuka and T. Majima, *J. Phys. Chem. B*, 2013, **117**, 13985–13992.
67 Q. Chen, J. Chen, C. Liang, L. Feng, Z. Dong, X. Song, G. Song and Z. Liu, *J. Controlled Release*, 2017, **263**, 79–89.
68 X. Song, C. Liang, H. Gong, Q. Chen, C. Wang and Z. Liu, *Small*, 2015, **11**, 3932–3941.
69 N. Zheng, Z. Zhang, J. Kuang, C. Wang, Y. Zheng, Q. Lu, Y. Bai, Y. Li, A. Wang and W. Song, *ACS Appl. Mater. Interfaces*, 2019, **11**, 18224–18232.
70 J. Jin, Y. Zhu, Z. Zhang and W. Zhang, *Angew. Chem., Int. Ed.*, 2018, **57**, 16354–16358.
71 N. Zheng, X. Li, S. Huangfu, K. Zia, R. Yue, H. Wu and W. Song, *Biomater. Sci.*, 2021, **9**, 4620–4638.
72 H. Y. Woo, B. Liu, B. Kohler, D. Korystov, A. Mikhailovsky and G. C. Bazan, *J. Am. Chem. Soc.*, 2005, **127**, 14721–14729.
73 C. M. Martin, *Annu. Rev. Phys. Chem.*, 2021, **72**, 617–640.
74 S. Wang, P. Huang, L. Nie, R. Xing, D. Liu, Z. Wang, J. Lin, S. Chen, G. Niu, G. Lu and X. Chen, *Adv. Mater.*, 2013, **25**, 3055–3061.
75 Y.-F. Ding, S. Li, L. Liang, Q. Huang, L. Yuwen, W. Yang, R. Wang and L.-H. Wang, *ACS Appl. Mater. Interfaces*, 2018, **10**, 9980–9987.
76 N. Zhang, F. Zhao, Q. Zou, Y. Li, G. Ma and X. Yan, *Small*, 2016, **12**, 5936–5943.
77 G. Leshem, M. Richman, E. Lisniansky, M. Antman-Passig, M. Habashi, A. Gräslund, S. K. T. S. Wärmländer and S. Rahimipour, *Chem. Sci.*, 2019, **10**, 208–217.
78 L. Feng, D. Tao, Z. Dong, Q. Chen, Y. Chao, Z. Liu and M. Chen, *Biomaterials*, 2017, **127**, 13–24.
79 Y.-X. Zhu, H.-R. Jia, Z. Chen and F.-G. Wu, *Nanoscale*, 2017, **9**, 12874–12884.
80 T. Mosmann, *J. Immunol. Methods*, 1983, **65**, 55–63.
81 H. Zhang, R. Huang, N.-K. V. Cheung, H. Guo, P. B. Zanzonico, H. T. Thaler, J. S. Lewis and R. G. Blasberg, *Clin. Cancer Res.*, 2014, **20**, 2182–2191.
82 K. Saimuang, K. Suttisintong, N. Kaewchangwat, E. Thanayupong, Y. Wongngam, P. Charoenphun, R. Wanotayan, A. Elaissari, S. Hongeng, D. Polpanich and K. Jangpatarapongsa, *RSC Adv.*, 2021, **11**, 25199–25206.
83 G. Villaverde, A. Baeza, G. J. Melen, A. Alfranace and M. Vallet-Regí, *J. Mater. Chem. B*, 2015, **3**, 4831–4842.
84 N. S. Potter, A. McLean, E. C. Bornowski, T. Hopkins, J. Luo, J. P. Wolfe, W. Qian and R. Kopelman, *ACS Mater. Lett.*, 2023, **5**, 2971–2977.
85 J. Schmitt, V. Heitz, A. Sour, F. Bolze, H. Ftouni, J.-F. Nicoud, L. Flamigni and B. Ventura, *Angew. Chem., Int. Ed.*, 2015, **54**, 169–173.
86 J. Schmitt, V. Heitz, A. Sour, F. Bolze, P. Kessler, L. Flamigni, B. Ventura, C. S. Bonnet and E. Tóth, *Chem. – Eur. J.*, 2016, **22**, 2775–2786.
87 L. Luo, Q. Zhang, Y. Luo, Z. He, X. Tian and G. Battaglia, *J. Controlled Release*, 2019, **298**, 99–109.